



Article

Butanediammonium Salt Additives for Increasing Functional and Operando Stability of Light-Harvesting Materials in Perovskite Solar Cells

Natalia N. Udalova ^{1,†} , Aleksandra K. Moskalenko ^{1,†}, Nikolai A. Belich ¹, Pavel A. Ivlev ¹, Andrey S. Tutantsev ¹, Eugene A. Goodilin ^{1,2} and Alexey B. Tarasov ^{1,2,*}

¹ Laboratory of New Materials for Solar Energetics, Department of Materials Science, Lomonosov Moscow State University, Lenin Hills, 119991 Moscow, Russia

² Department of Chemistry, Lomonosov Moscow State University, Lenin Hills, 119991 Moscow, Russia

* Correspondence: alexey.bor.tarasov@yandex.ru

† These authors contributed equally to this work.

Abstract: Organic diammonium cations are a promising component of both layered (2D) and conventional (3D) hybrid halide perovskites in terms of increasing the stability of perovskite solar cells (PSCs). We investigated the crystallization ability of phase-pure 2D perovskites based on 1,4-butanediammonium iodide (BDAl₂) with the layer thicknesses $n = 1, 2, 3$ and, for the first time, revealed the presence of a persistent barrier to obtain BDA-based layered compounds with $n > 1$. Secondly, we introduced BDAl₂ salt into 3D lead-iodide perovskites with different cation compositions and discovered a threshold-like nonmonotonic dependence of the perovskite microstructure, optoelectronic properties, and device performance on the amount of diammonium additive. The value of the threshold amount of BDAl₂ was found to be $\leq 1\%$, below which bulk passivation plays the positive effect on charge carrier lifetimes, fraction of radiative recombination, and PSCs power conversion efficiencies (PCE). In contrast, the presence of any amount of diammonium salt leads to the sufficient enhancement of the photothermal stability of perovskite materials and devices, compared to the reference samples. The performance of all the passivated devices remained within the range of 50 to 80% of the initial PCE after 400 h of continuous 1 sun irradiation with a stabilized temperature of 65 °C, while the performance of the control devices deteriorated after 170 h of the experiment.

Keywords: perovskite solar cells; hybrid halide perovskites; exploitation stability; defect passivation; diammonium cations; layered lead halide perovskites; bulk passivation; BDAl₂; 1,4-butanediammonium iodide



Citation: Udalova, N.N.; Moskalenko, A.K.; Belich, N.A.; Ivlev, P.A.; Tutantsev, A.S.; Goodilin, E.A.; Tarasov, A.B. Butanediammonium Salt Additives for Increasing Functional and Operando Stability of Light-Harvesting Materials in Perovskite Solar Cells. *Nanomaterials* **2022**, *12*, 4357. <https://doi.org/10.3390/nano12244357>

Academic Editor: Elias Stathatos

Received: 12 November 2022

Accepted: 3 December 2022

Published: 7 December 2022

Publisher's Note: MDPI stays neutral with regard to jurisdictional claims in published maps and institutional affiliations.



Copyright: © 2022 by the authors. Licensee MDPI, Basel, Switzerland. This article is an open access article distributed under the terms and conditions of the Creative Commons Attribution (CC BY) license (<https://creativecommons.org/licenses/by/4.0/>).

1. Introduction

The steep progress of perovskite photovoltaics over the last decade relies mainly on the impressive growth of record power conversion efficiencies up to 25.7%, being almost as high as the record PCE of monocrystalline silicon-based solar cells (26.1%) [1]. At the same time, the long-term stability of PSCs is still far from the target value of 20–25 years [2], despite significant progress in this field driven by a number of approaches like perovskite compositional engineering [3], dopant-free hole-transporting materials [4], barrier layers [5], the application of 2D perovskites [6], and 2D/3D heterostructures [7], as well as the control of surface and bulk defects in perovskite materials and interfaces through passivation with various organic or inorganic compounds [8]. Organic ammonium salts have been successfully used in the last three approaches [9–11]. The most prominent member of these additives is the n-butylammonium (BA⁺) cation, which forms a homologous row of layered (BA)₂(MA)_{n-1}Pb_nX_{3n+1} perovskites with a wide range of n [12]. The use of n-butylammonium-based 2D/3D heterostructures allows to create devices with record open-circuit voltage [13] and outstanding exploitation stability [14]. Along with such clear

advantages, monoammonium cations demonstrate a tendency of dynamical evolution of 2D/3D interfaces under heating and light illumination, leading to PSC instability and loss of performance [15,16].

Diammonium cations should be considered as a promising alternative with various advantages, including their much lower deprotonation ability, the absence of van der Waals gaps in 2D perovskite structures and possible influence on perovskite grain and domain interconnections [6,17]. Indeed, a direct stability comparison of PSCs based on monoammonium and diammonium cations revealed the superiority of diammonium counterparts used as either spacer cations in 2D perovskites [6,18] or passivating agents in 3D structures [19]. It is known that different chemical structures and carbon chain lengths of diammonium cations play a crucial role in PSCs performance and stability [20–22], thus demanding a proper selection of organic compounds with desired functional groups. One of the record PSC stabilities over 5000 h under continuous 1 sun illumination has been achieved so far by using 2D perovskites with a 1,3-propanediammonium (PDA) spacer cation and cesium co-doping [23]. On the other hand, a direct comparison of diammonium cations with different chain lengths within 2D perovskites, provided by Zheng et al., revealed the superior performance and stability of PSCs with a 1,4-butanediammonium (BDA) spacer cation, as compared to PDA-based devices [21]. The same trend was reported for the case of surface passivation with diammonium halides, where BDAI₂ demonstrated better performance than PDAI₂ [22]. These results are reliable, since PDAI₂ (in contrast to BDAI₂) forms a non-perovskite structure with the empirical formula [PDAPbI₄]₁₅•[PDAI₂] [24]. Therefore, 1,4-butanediammonium appears to be a more promising alternative to shorter PDA²⁺ cations and other diammonium counterparts. However, there are very few works regarding the use of BDA²⁺ in PSCs and the available results are controversial in terms of the ability to crystallize different members of the 2D (BDA)(MA)_{n-1}Pb_nI_{3n+1} compositional row; BDA²⁺ localization in 3D perovskites; the role of BDA²⁺ additives in performance and photothermal stability of perovskite solar cells.

Here, we provided a systematic study on the use of 1,4-butanediammonium diiodide (BDAI₂) either as a spacer cation in 2D (BDA)(MA)_{n-1}Pb_nI_{3n+1} perovskites or as a passivating agent in 3D MA_{0.25}FA_{0.75}PbI₃ and FA_{0.85}Cs_{0.15}PbI₃ counterparts to define the most effective method of introducing BDAI₂ into light-harvesting materials in perovskite solar cells.

2. Materials and Methods

Materials. Methylammonium iodide (CH₃NH₃I = MAI; 99%, Dyesol, Queanbeyan, Australia), formamidinium iodide (CH(NH₂)₂I = FAI; ≥99%, Dyesol), cesium iodide (CsI; >99%, TCI, Tokyo, Japan), butane-1,4-diammonium iodide (INH₃(CH₂)₄NH₃I = BDAI₂, ≥99%, Dyesol), lead iodide (PbI₂; >98%, Lanhit, Moscow, Russia), n-butylammonium iodide (C₄H₉NH₃I = BAI; ≥99%, Dyesol), chlorobenzene (C₆H₅Cl = CB; anhydrous, 99.8%, Sigma-Aldrich, St. Louis, MO, USA), dimethylsulfoxide ((CH₃)₂SO = DMSO; anhydrous, ≥99.9%, Sigma-Aldrich), N,N-dimethylformamide (HCON(CH₃)₂ = DMF; anhydrous, 99.8%, Sigma-Aldrich), toluene (anhydrous, 99.8%, Sigma-Aldrich), propylene carbonate (≥99.9%, Sigma-Aldrich), methylammonium chloride (CH₃NH₃Cl = MACl; ≥99%, Merck, Rahway, NJ, USA), fluorine-doped tin oxide (FTO) substrates (FTO-coated glass slide, ~7 Ω/sq, Sigma-Aldrich), Spiro-OMeTAD (99.5%, Sigma-Aldrich), 4-tert-butylpyridine (TBP, >96%, Sigma-Aldrich), LiTFSI (99.8%, Sigma-Aldrich), anhydrous acetonitrile (99.8% Alfa Aesar, Haverhill, MA, USA), FK209 (tris(2-(1H-pyrazol-1-yl)-4-tert-butylpyridine)cobalt(III) tris[bis(trifluoromethane)sulfonimide], 98%, Sigma-Aldrich), Au (99.95%), molecular iodine, molybdenum trioxide (MoO₃, 99.99%, Lanhit), titanium (IV) isopropoxide (97%, Sigma Aldrich), acetilacetone (99.5%, Sigma Aldrich), isopropyl alcohol (99.8%, Component-Reactiv), mercaptoacetic acid (98%, Acros) and SnCl₂·2H₂O (99.99%, Lanhit) were commercially purchased.

Synthesis of 2D perovskite crystals. Crystals with the following nominal compositions were synthesized by the solution method described in [25]: BA₂PbI₄, BA₂MAPb₂I₇,

(BDA)PbI₄, and (BDA)MAPb₂I₇. A 1.5 M stoichiometric solution of the corresponding halide salts in a mixture of propylene carbonate and hydroiodic acid was kept at a constant temperature of 70 °C for 8 h. A (BDA)MAPb₂I₇ solution was also prepared with a 1.5 M and 0.1 M concentration to study the effect of concentration on 2D perovskite phase composition. Crystallization in the (BDA)MAPb₂I₇ solution with 25, 50, 75, and 100% excess of MAI, with respect to Pb content, was achieved with 1.5 M solutions using the same method. All the resulting crystals were dried, ground, and studied by powder X-ray diffraction.

Crystallization of (BDA)MAPb₂I₇ and (BDA)MA₂Pb₃I₁₀ using an equilibrium system with a transfer mediator. To study the equilibrium phases in the (BDA)(MA)_{n-1}Pb_nI_{3n+1} system with n = 2 and 3, we carried out the following experiment: the mixtures of solid-state BDAI₂ + MAI + PbI₂ precursors with (BDA)(MA)Pb₂I₇ (n = 2) and (BDA)(MA)₂Pb₃I₁₀ (n = 3) overall compositions were thoroughly ground in an argon-filled glove box (<10 ppm O₂; 0.1 ppm H₂O) and then dispersed in dry toluene with a 5% amount of molecular iodine as a mass-transfer agent. The 5% amount of iodine was estimated with respect to the total lead amount. The prepared solid–liquid mixtures were continuously stirred and heated at 70 °C for 7 days to achieve thermodynamic equilibrium. After the resulting powders were washed several times with pure toluene, they were dried, and again ground in the glove box with dry air (<20% RH) just before XRD analysis.

Deposition of 3D perovskite films. MA_{0.25}FA_{0.75}PbI₃ perovskite films were prepared from 1.5 M solutions of MAI, FAI, PbI₂ in stoichiometric molar ratios with 15% excess of MAI in DMF/DMSO (4:1 v/v) via 1-step antisolvent spin-coating in an inert glove box. Spin-coating was performed at 6000 rpm for 30 s, where 100 µL of chlorobenzene was added dropwise at the 5th second of rotation. The following annealing step was performed at 125 °C for 20 min: FA_{0.85}Cs_{0.15}PbI₃ perovskite films were prepared by the same method from 1.3 M stoichiometric solution of FAI, CsI, and PbI₂ in DMF/DMSO (4:1 v/v). The spin-coating method was the same as in the previous example, except for the addition of CB at the 15th second of rotation. Annealing was also performed for 20 min at 125 °C.

Bulk passivation of both perovskite compositions was carried out following the addition of 0.2, 0.5, 1, 2.5 and 5 mol.% BDAI₂ with respect to Pb content, to the initial perovskite solutions by mixing two perovskite solutions with 0 and 5% BDAI₂ in the volume ratios that corresponded to the resulting amount of the additive.

Fabrication of perovskite solar cells. FTO-coated glass substrates were patterned via chemical etching (Zn powder + 4 M HCl) and then sequentially cleaned with detergent (2% Hellmanex solution), distilled water, and the prepared solution of concentrated H₂SO₄ + 30% H₂O₂ in a volume ratio of 3:1 for 10 min. After this, the substrates were washed in deionized water, dried by N₂ gas flow, and immediately transferred onto a hotplate for the deposition of the blocking TiO₂ layer. A compact TiO₂ layer was formed by spray pyrolysis at 450 °C. The precursor solution was prepared by mixing 900 µL of titanium (IV) isopropoxide, 600 µL of acetilacetone and 50 mL of isopropyl alcohol. After spraying, the substrates were annealed for 60 min at 450 °C and then left to cool down. The deposition of the SnO₂ layer was carried out according to the method stated in ref. [26]. Shortly after, 0.625 g of urea was dissolved in 500 mL of deionized water, followed by the addition of 10 µL of mercaptoacetic acid and 0.5 mL of 37% HCl. Finally, 0.1 g of SnCl₂·2H₂O was dissolved in the above-mentioned solution. The glass/FTO/c-TiO₂ substrates were previously treated by ozone with UV/ozone cleaner (Osilla) for 15 min, placed vertically into a glass with the as-prepared solution, and then stored in a laboratory oven at 70 °C for 3 h. After SnO₂ deposition, the substrates were rinsed with deionized water and sonicated for 2 min to remove large agglomerates from the SnO₂ film surface. Finally, the dried substrates were transferred onto a hotplate and annealed at 180 °C for 1 h. FA_{0.85}Cs_{0.15}PbI₃ + x% BDAI₂ perovskite films (where x = 0.25, 0.5, 1, 2.5, and 5%) were deposited on FTO/c-TiO₂/SnO₂ substrates, according to the previously described protocol. The spiro-OMeTAD solution was prepared by dissolving 60 mg of Spiro-OMeTAD in 598 µL of CB with 21.6 µL of TBP, 12 µL of 1.8 M solution of LiTFSI in anhydrous acetonitrile, and 4.8 µL of 0.25 M solution of co-complex FK209 in anhydrous acetonitrile. Deposition of 28 mkl of doped

spiro-OMeTAD solution was carried out at 4000 rpm in an inert glove box. Finally, an Au electrode with ~80 nm thickness was deposited by thermal evaporation (base pressure 10^{-5} Torr) through a shadow mask.

Encapsulation of perovskite solar cells. The method for the encapsulation of PSCs was provided by ref. [27]. At the first stage, a 150–200 nm layer of molybdenum trioxide (MoO_x) was thermally evaporated under a high vacuum ($P = 1 \times 10^{-5}$ mbar) on top of the as-prepared PSCs. The deposition rate was monitored via QSM sensors and maintained at 0.4–0.7 Å/s. After the evaporation of the capping layer, the solar cells were immediately transferred into a nitrogen-filled glovebox. The second encapsulation step was carried out with commercially available UV-curable polymers (“Nano Clear” by FunToDo) and a cover glass slide. For this step, 5–7 μL of epoxy was dispensed onto an active area of each device and covered by a glass slide. Immediately after this, the photopolymerization of the epoxy was carried out via UV light exposure (10 W InGaAlN LED; $\lambda = 365\text{--}375$ nm) for 1–2 min.

Perovskite solar cell characterization and stability measurements. The current density–voltage (J–V) characteristics of solar cells were measured with a Keithley series 2450 source meter under a simulated sun AM 1.5 G (ORIEL LSH-7320 ABA LED Solar Simulator) with custom-built python-based software. The light intensity was calibrated to 1 sun (AM1.5, 100 mWcm^{-2}) by unfiltered Si reference cells calibrated by Newport.

The long-term photostability of encapsulated PSCs under ambient conditions was achieved using an unfiltered sulfur plasma lamp (LG PSH 0731B), calibrated with Si reference cells to a $100 \pm 10 \text{ mW/cm}^2$ power density. To maintain the desired device temperature, PSCs were placed onto a custom-built copper stage that was consistently heated to 65 °C. MPPT was performed using a standard perturb and observe algorithm and the voltage was updated every 5 min with a 10 mV step by a homemade electronic board with 16-channel MPPT capability.

X-Ray powder diffraction. XRD analysis was performed using a Bruker Advance D8 diffractometer with Bragg–Brentano geometry and Cu $K\alpha$ radiation ($\lambda = 15,418$ Å). XRD patterns were recorded in the 3–35° 2θ range with 0.1 s per dot and a 0.02° step.

SEM. Scanning electron microscopy (SEM) was performed on a Zeiss Supra 40 microscope with an accelerating voltage of 1–5 kV.

PL spectroscopy. PL spectra were recorded via a home-built setup based on Thorlabs components with a 405 nm excitation laser, 10x focusing objective lens, and an Ocean Optics Flame spectrometer. The laser power was ~200–210 μW , and the laser spot size was ~10 μm .

Time-resolved photoluminescence spectroscopy. Time-resolved photoluminescence spectroscopy (TRPL) was performed with a laser pulse frequency of 1000 kHz and a single pulse time of 30 ps. PL decay curves were recorded on a calibrated HMP-100-50 single-photon detector (Becker and Hickl, Germany), equipped with an SPC-150 module. The PL decay curves were processed using the SPC Image software (Becker and Hickl) and OriginPro. To approximate the decay curves, we used the sum of two exponential decay functions, which was as follows: $\tau_{\text{avg}} = (A_1\tau_1 + A_2\tau_2)/(A_1 + A_2)$, where A_i and τ_i are the amplitude and lifetime of charge carriers for the i th component of the decay curve, respectively.

Photostability study of perovskite films. The photostability study of perovskite films was carried out according to the protocol described in [28]. The perovskite films on FTO substrates were irradiated with a white LED with 100 mW/cm^2 power density in an argon-filled glove box (<10 ppm O_2). All perovskite films were irradiated from the substrate side to minimize the interference of defective perovskite surfaces in light-induced degradation [29]. The characterization of perovskite films was periodically provided by PL spectroscopy under an inert atmosphere. The comparison of the photostability of different perovskite samples was carried out based on normalized PL intensity values as a function of the light-soaking time.

3. Results and Discussion

The synthesis of higher n members of $(\text{BDA})(\text{MA})_{n-1}\text{Pb}_n\text{I}_{3n+1}$ 2D perovskites has not been yet clearly presented, while published XRD and optical spectroscopy data are very contradictory [18,30]. Often, authors discuss the problem of the solution synthesis of phase-pure $(\text{BDA})(\text{MA})_{n-1}\text{Pb}_n\text{I}_{3n+1}$ with $n > 1$, demonstrating the formation of multiple-phase samples with the prevailing $(\text{BDA})\text{PbI}_4$ and/or 3D perovskite phases [31–33]. An analysis of the open access 2D perovskites database [34] reveals that only $(\text{BDA})\text{PbI}_4$ ($n = 1$) crystallographic data have been reported [35].

To clarify this issue, we tried to synthesize $(\text{BDA})(\text{MA})_{n-1}\text{Pb}_n\text{I}_{3n+1}$ layered perovskites with $n = 2$ and 3 using the following two methods: crystallization from a 1.5 M solution of $n\text{PbI}_2 + (n-1)\text{MAI} + \text{BDAI}_2$ in an HI + propylene carbonate mixture, as previously reported in [25], and slow crystallization using an equilibrium system with a transfer mediator. At first, we achieved the solution synthesis of single crystals for $(\text{BDA})(\text{MA})_{n-1}\text{Pb}_n\text{I}_{3n+1}$ and $(\text{BA})_2(\text{MA})_{n-1}\text{Pb}_n\text{I}_{3n+1}$ (BA—butylammonium) compositions with $n = 1$ and 2 (Figure 1). In the case of BA-based solutions, high-quality single crystals with target n numbers were successfully obtained (Figure 1A,B), while only the $(\text{BDA})\text{PbI}_4$ phase (yellow crystals) was able to crystallize from BDA-based solutions, regardless of the initial precursors' stoichiometry (Figure 1C,D). This behavior of the system was previously explained by the much lower solubility of the $n = 1$ member, due to the strong electrostatic affinity of diammonium cations towards inorganic perovskite-like layers [31]. Additional attempts to crystallize $(\text{BDA})(\text{MA})\text{Pb}_2\text{I}_7$ perovskites from a diluted 0.1 M solution also resulted in the formation of $(\text{BDA})\text{PbI}_4$ phases (Figure S1). Hypothetically, the excess of MAI in the solution that corresponds to the $(\text{BDA})(\text{MA})\text{Pb}_2\text{I}_7$ composition could shift the equilibrium of the system towards the crystallization of the $n = 2$ member. However, according to our experimental results, the BDA-based solution system does not respond to the variation in MAI:BDAI₂ stoichiometry up to 2:1 (100% excess of MAI), thus preserving $(\text{BDA})\text{PbI}_4$ phase composition (Figure S2).

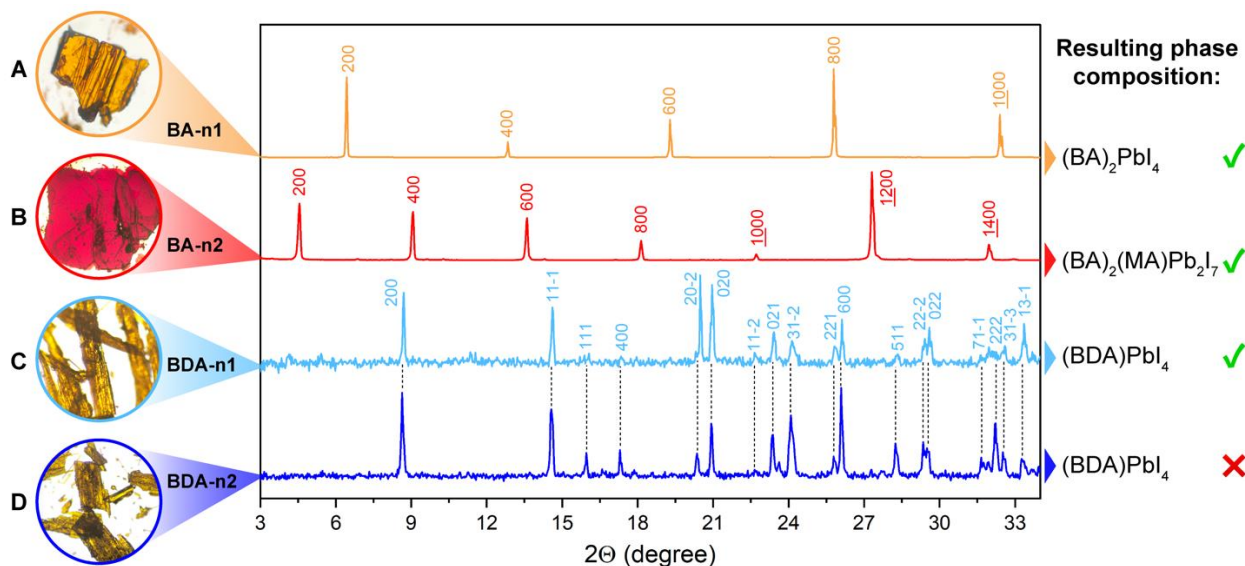


Figure 1. Optical photographs of single crystals, synthesized from solutions relevant to $(\text{BA})_2\text{PbI}_4$ (A), $(\text{BA})_2(\text{MA})\text{Pb}_2\text{I}_7$ (B), $(\text{BDA})\text{PbI}_4$ (C), $(\text{BDA})(\text{MA})\text{Pb}_2\text{I}_7$; (D) perovskite compositions and corresponding powder XRD patterns. On the right, the actual phase composition of each sample is given, indicating the failure to obtain the $(\text{BDA})(\text{MA})\text{Pb}_2\text{I}_7$ compound.

To study the thermodynamic equilibrium in the $(\text{BDA})(\text{MA})_{n-1}\text{Pb}_n\text{I}_{3n+1}$ system, we carried out the following experiment: the mixtures of solid-state $\text{BDAI}_2 + \text{MAI} + \text{PbI}_2$ precursors with $(\text{BDA})(\text{MA})_2\text{Pb}_3\text{I}_{10}$ ($n = 3$) and $(\text{BDA})(\text{MA})\text{Pb}_2\text{I}_7$ ($n = 2$) overall compositions were thoroughly ground in an inert glove box and then dispersed in dry toluene

with a 5% amount of molecular iodine as a mass-transfer agent (Figure 2A). The mass transfer proceeds through the liquid media via the formation of liquid alkylammonium polyiodides [36,37], which play the role of highly reactive intermediate phases that quickly yield hybrid iodoplumbates with the highest thermodynamic stability. The grinding stage can initiate the solid-state formation of layered perovskite phases, which was reported earlier as a more perspective preparation method for diammonium-based 2D perovskites than solution synthesis [31]. The prepared solid–liquid mixtures were continuously stirred and heated at 70 °C for 7 days; after this, the resulting powders were washed several times with pure toluene, dried, and again ground just before XRD analysis. Diffraction patterns of the resulting powder samples are given in Figure 2B, demonstrating that the mixtures of (BDA)PbI₄ and MAPbI₃ with some amount of unreacted PbI₂ formed instead of (BDA)(MA)₂Pb₃I₁₀ and (BDA)(MA)Pb₂I₇ phases in both cases. A relative amount of (BDA)PbI₄ and MAPbI₃ phases correlates with the initial stoichiometry; the (BDA)PbI₄ phase dominates the (BDA)(MA)Pb₂I₇ sample (Figure 2B(2)), while 3D perovskite is the main product for the (BDA)(MA)₂Pb₃I₁₀ sample (Figure 2B(1)).

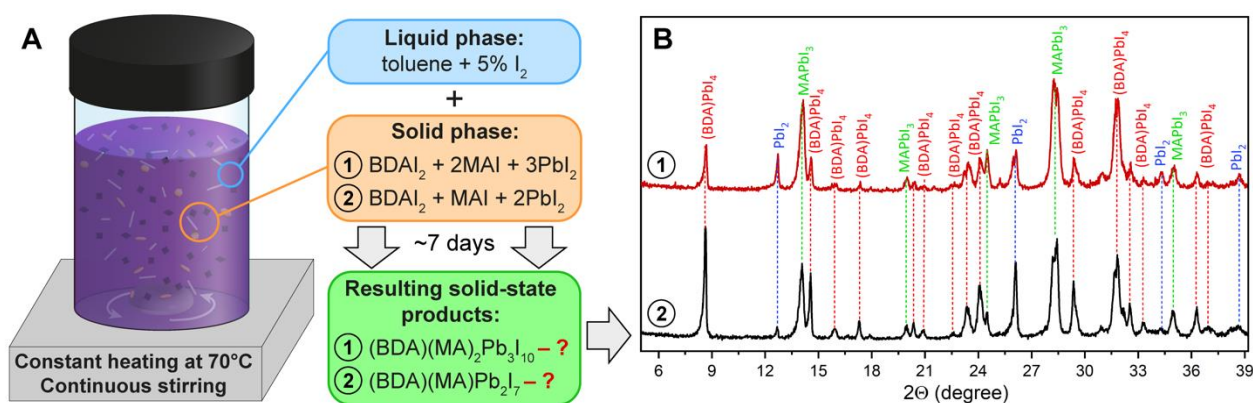


Figure 2. (A) The scheme of the experimental setup for the study of reactivity of the mixture of BDAI₂ + MAI + PbI₂ powders with component ratios corresponding to (BDA)(MA)₂Pb₃I₁₀ (1) and (BDA)(MA)Pb₂I₇ (2). The role of component transfer media in 5% I₂ solution in dry toluene. (B) XRD patterns of the resulting solid-state products after 7 days of continuous heating and stirring of the initial precursor mixtures. Each peak is labeled by the corresponding phase: (BDA)PbI₄ (red), PbI₂ (blue); MAPbI₃ (green).

Considering these results along with previously reported data, we conclude that the formation of a light-absorbing layer based on phase-pure 2D (BDA)(MA)_{n-1}Pb_nI_{3n+1} perovskite is unfavorable. On the other hand, passivation of 3D perovskites with BDAI₂ appears to be more beneficial and can be accompanied by the formation of either (BDA)PbI₄ phases or BDA²⁺ layers at the interfaces and/or perovskite intra and intergrain boundaries (GBs). In the case of surface passivation, the formation of (BDA)PbI₄ phases on the perovskite surface was previously reported [38–40], but the effect of bulk passivation with BDAI₂ on the structure and optical properties of 3D perovskites has not been fully discussed, despite the potential for more efficient passivation of cation and anion vacancies throughout the thickness of the perovskite film. To clarify this issue, we performed bulk passivation of MA_{0.25}FA_{0.75}PbI₃ (MAFAPbI₃) and FA_{0.85}CS_{0.15}PbI₃ (FACsPI) perovskite films with different amounts of BDAI₂ and studied the effect of passivation on the morphology, crystal structure, optical properties, and photostability of perovskite films, as well as PSCs. The use of mixed-cation perovskites was motivated by their higher PCE and stability compared to the conventional MAPbI₃ composition [41–44]. The amount of diammonium additives in the perovskite solution varied in a wide range from trace 0.025 wt.% [17] to 3–8% [20,45]; therefore, we chose the following BDAI₂ concentrations for 3D perovskite bulk passivation: 0.25, 0.5, 1, 2.5, and 5%.

According to the XRD data of the $\text{MA}_{0.25}\text{FA}_{0.75}\text{PbI}_3 + x\%$ BDAI_2 samples (Figure 3A), no phase impurities, such as $(\text{BDA})\text{PbI}_4$ or delta polytypes of FAPbI_3 , formed after the introduction of BDAI_2 into the material. The same behavior was observed for the $\text{FACsPI} + x\%$ BDAI_2 samples (Figure S3). Interplanar distances in the perovskite lattice were also not affected by the diammonium additive (Figure 3B). Evidently, such small amounts of additives would not be detected by XRD; however, we observed the widening of diffraction reflexes along with an increased amount of the BDAI_2 additive, as shown in Figure 3B for the (100) perovskite reflex. This seems to correlate with the monotonic decrease in the average grain size from 407 ± 149 nm for the reference MAFAPI sample, down to 188 ± 46 nm for $\text{MAFAPI} + 5\%$ BDAI_2 (Figure 3C–F). In the case of FACsPI perovskite composition, we also observed a pronounced decrease in grain size with the addition of $\geq 1\%$ BDAI_2 , while 0.25% of diammonium salt does not noticeably affect the perovskite morphology (Figure S4). The decrease in grain size with the BDAI_2 additive may be due to the preferential localization of diammonium cations on the GBs instead of the perovskite lattice, since a too large BDA^{2+} cation cannot be incorporated into 3D perovskites without severe lattice distortions. Similar trends with decreasing grain size during perovskite passivation with diammonium salts are reported elsewhere [45,46].

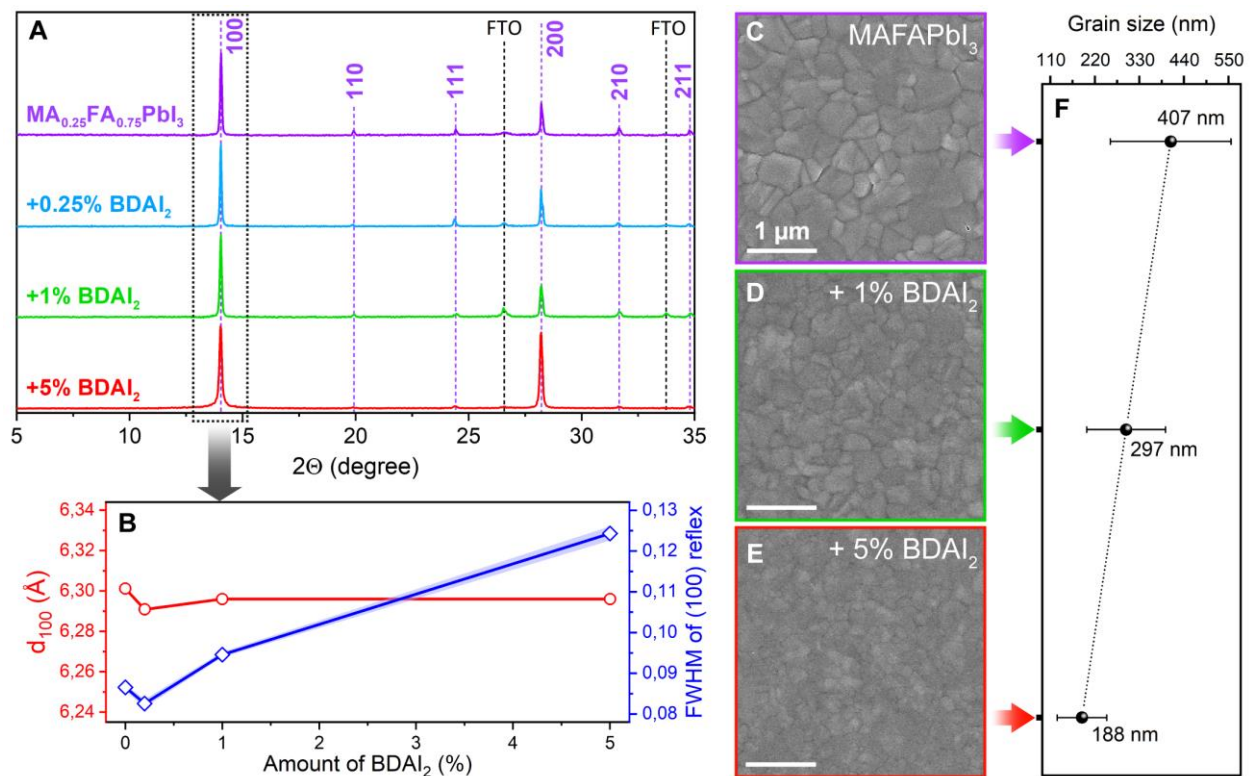


Figure 3. (A) XRD patterns of $\text{MA}_{0.25}\text{FA}_{0.75}\text{PbI}_3$ perovskite films with a different amount of BDAI_2 additive. (B) Interplanar distance (red) and FWHM (blue) of (100) perovskite reflex as a function of BDAI_2 amount. (C–E) Top-view SEM images of MAFAPI perovskite films without additive (C), with 1% BDAI_2 (D), and with 5% BDAI_2 (E). The scale bars are 1 μm . (F) Average grain size of corresponding perovskite films with different BDAI_2 contents.

The optoelectronic properties of perovskite films also depend strongly on the BDAI_2 amount. Time-resolved photoluminescence (TRPL) data of the $\text{MAFAPI} + x\%$ BDAI_2 samples reveal a dramatic decrease in the average charge carrier lifetimes t_m from 97.2 ns for the reference perovskite sample down to 20.6 ns and 11.3 ns for the samples with 1% and 5% BDAI_2 , respectively (Figure 4A). The lifetime decrease is accompanied by the growing proportion of fast decay components (t_1 in the inset table in Figure 4A), which are usually associated with trap-assisted recombination on the surface and at the GBs. In

contrast, a small amount of diammonium additive (0.25% BDAI₂) leads to an increase in the average lifetime t_m up to 124.1 ns and a simultaneous rise in the slow decay component t_2 , which is thought to originate from perovskite bulk [47]. Steady-state photoluminescence (PL) data of MAFAPI + $x\%$ BDAI₂ correlate with the TRPL decay curves; perovskite PL intensity increases with 0.25% BDAI₂ with respect to the reference MAFAPI sample, but is progressively quenched with the further addition of 1, 2.5, and 5% BDAI₂ (Figure 4B). Interestingly, FACsPI perovskite composition has higher “tolerance” to the BDAI₂ additive, with a gradual increase in PL intensity up to 1% BDAI₂ (Figure 4C). After overcoming the threshold level of 1% BDAI₂, FACsPI films also suffer from a dramatic loss of PL intensity, which is accompanied by the widening of emission lines (Figure 4D, red lines). In addition, the center of the PL peaks (X_C) of both perovskite compositions shifts to shorter wavelengths up to 14 nm at the maximum BDAI₂ content of 5% (Figure 4D, blue lines). Similar trends are observed for the FACsPI + $x\%$ BDAI₂ samples by optical absorption spectroscopy (Figure S5). This slight increase in the perovskite bandgap could be explained by the distortions of the inorganic [PbI₃]⁻ sublattice [46], which is predominantly located at grain boundaries [48], the proportion of which becomes higher with the increasing amount of diammonium additive according to the morphological observations (Figures 3C–F and S4).

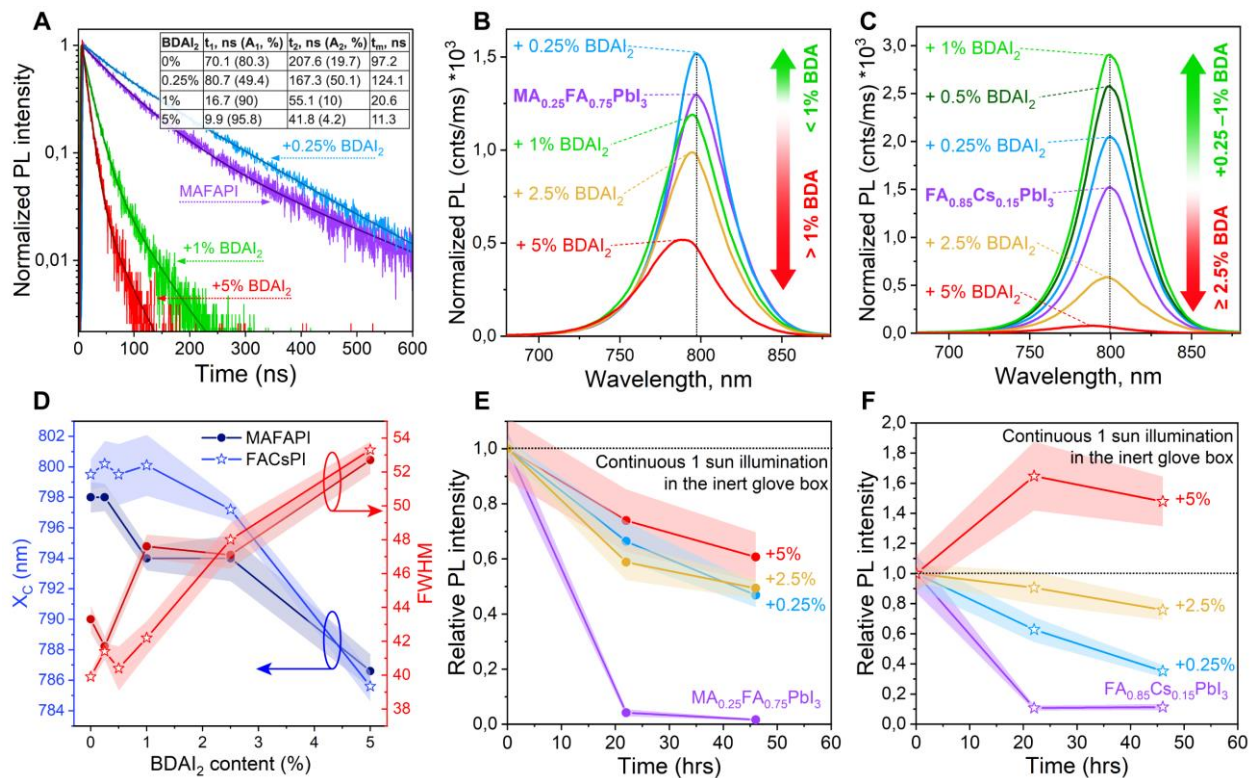


Figure 4. (A) Time-resolved PL decay curves of MA_{0.25}FA_{0.75}PbI₃ + $x\%$ BDAI₂ films. Estimated charge carrier lifetimes (t_1 and t_2 with corresponding relative amplitudes A_1 and A_2 , and average lifetime t_m) are given in the inset table in (A). (B,C) Steady-state PL spectra of MA_{0.25}FA_{0.75}PbI₃ + $x\%$ BDAI₂ (B) and FA_{0.85}Cs_{0.15}PbI₃ + $x\%$ BDAI₂ (C) films. (D) Graphical illustration of PL peak positions (X_C) and widths (FWHM) as a function of BDAI₂ content for both MAFAPI (—●—) and FACsPI (—☆—) samples. (E,F) Photostability of MAFAPI (E) and FACsPI (F) films with different BDAI₂ contents as an evolution of PL intensity, under continuous 1 sun irradiation in inert glove box.

The comparative study of long-term photostability of MAFAPI and FACsPI perovskite films was carried out in accordance with the previously reported approach based on continuous light soaking of perovskite films in an inert glove box and periodic registration of PL signals [28]. The resulting evolution of relative PL intensity of the perovskite samples, normalized to the first measurements, is given in Figure 4E for MAFAPI and Figure 4F for

FACsPI compounds. The reference samples of both perovskites undergo a dramatic drop in PL intensity after 22 h of light soaking, as 0.25% of the BDAI₂ additive is sufficient to slow down the degradation process. The further increase in the BDAI₂ content up to 5% reveals a different response of MAFAPI and FACsPI perovskites' photostability to bulk passivation. The MAFAPI films show no further stabilization of the PL signal, demonstrating threshold-like behavior and the effectiveness of small amounts of diammonium salt for the improvement of both perovskite optoelectronic properties and long-term photostability. In turn, the FACsPI perovskite composition appears to be more sensitive to BDAI₂ content with a photostability that is proportional to the passivator amount (Figure 4F). FACsPI + 5% BDAI₂ demonstrates enhancement of the PL signal under continuous 1 sun illumination, while 2.5% of the additive preserves 80% of the initial PL intensity. These observations, together with the steady-state PL data, motivate us to choose the FACsPI perovskite composition with BDAI₂ bulk passivation as a light absorbing material in PSCs.

Hence, we investigated the influence of BDAI₂ passivation on FACsPI-based PSC performance and stability. The devices were assembled with the following planar architecture: FTO/c-TiO₂/SnO₂/perovskite/spiro-OMeTAD/Au and encapsulated in an inert glove box with MoO_x and epoxy resin in accordance with ref. [27]. The analysis of J–V curves (Figure 5A), PCE statistics (Figure 5B) and dynamics of other PSC working parameters (Figure 5C) as a function of BDAI₂ content reveals again the threshold-like behavior of the devices, where >1% BDAI₂ content initiates an almost order of magnitude PCE decrease for the 5% BDAI₂ additive, while ≤1% BDAI₂ has a slight effect on PCE (Figure 5A,B). A comparative analysis of basic PSC working parameters, including fill factor (FF), open circuit voltage (V_{OC}), short circuit current density (J_{SC}), and PCE (Figure 5C), normalized to the corresponding values of the control devices, reveals a strong correlation of PCE with J_{SC}, which agrees with the previously observed decrease of the average grain sizes and charge carrier lifetimes in perovskite films (Figures 3C–F and S4). The absolute values of all the listed parameters are given in the Supporting Information (Figure S6). The fill factor of PSCs tends to monotonically decrease, losing up to 30% of the initial FF value, in contrast to the increasing V_{OC}. Usually, a V_{OC} increase is explained by the reduction in the trap densities in the device [49], and also correlates with a slight widening of the perovskite bandgap with the addition of ≥1% BDAI₂ (Figures S5 and 4D).

We also estimated the series and shunt resistances from quasi-steady-state J–V curves and revealed similar trends, as both resistances tended to increase with growing amounts of diammonium additive (Figure S7). It means that BDAI₂ passivation exerts two opposite effects on hybrid perovskite materials and devices, including the positive effect of decreasing the number of shunts and the negative effect of decreasing the electric conductivity in the devices.

The long-term stability tests of encapsulated PSCs were performed under constant ~100 mW/cm² white light illumination and a stabilized temperature of 65 °C, using a maximum power point tracking (MPPT) regime in an ambient environment. The resulting stabilized power outputs (SPO) of the best devices with different BDAI₂ contents, normalized to the first measurements, are shown in Figure 5D. The reference FACsPI-based solar cell undergoes rapid irreversible degradation between 140 and 190 h of the experiment, being the least stable device in the row. This is accompanied by the severe deterioration of the initial perovskite morphology (Figure 5E). In contrast, all passivated solar cells demonstrate superior stability, remaining within the 50 to 80% range of the initial SPO after 400 h of continuous photothermal aging. The least stable device within this group appears to be FACsPI + 0.25% BDAI₂, while all other samples with more diammonium content demonstrate higher stability. The absolute values of SPO are provided in SI (Figure S8). Importantly, the presence of BDAI₂ even at a low level of 0.25% protects the perovskite morphology and phase from degradation on a timescale of 400 h, which is illustrated by the comparative SEM images in Figure 5E. The enlarged version of these microscopy data is given in Figure S9. Interestingly, we observed unusual behavior of the SPO during the first 50 h of the light-soaking experiment with a pronounced drop in the device performance,

which was restored to the initial value (in the case of 1% BDAI₂) or to 80–90% of the initial SPO (for reference, 0.25%, and 0.5% BDAI₂ samples) (Figure 5D). In the literature, similar SPO evolution was previously reported for n-i-p PSCs architectures by Jung et al. [50] and Bai et al. [51] without, however, any explanation. Notably, high enough BDAI₂ contents ($\geq 2.5\%$) diminish this effect.

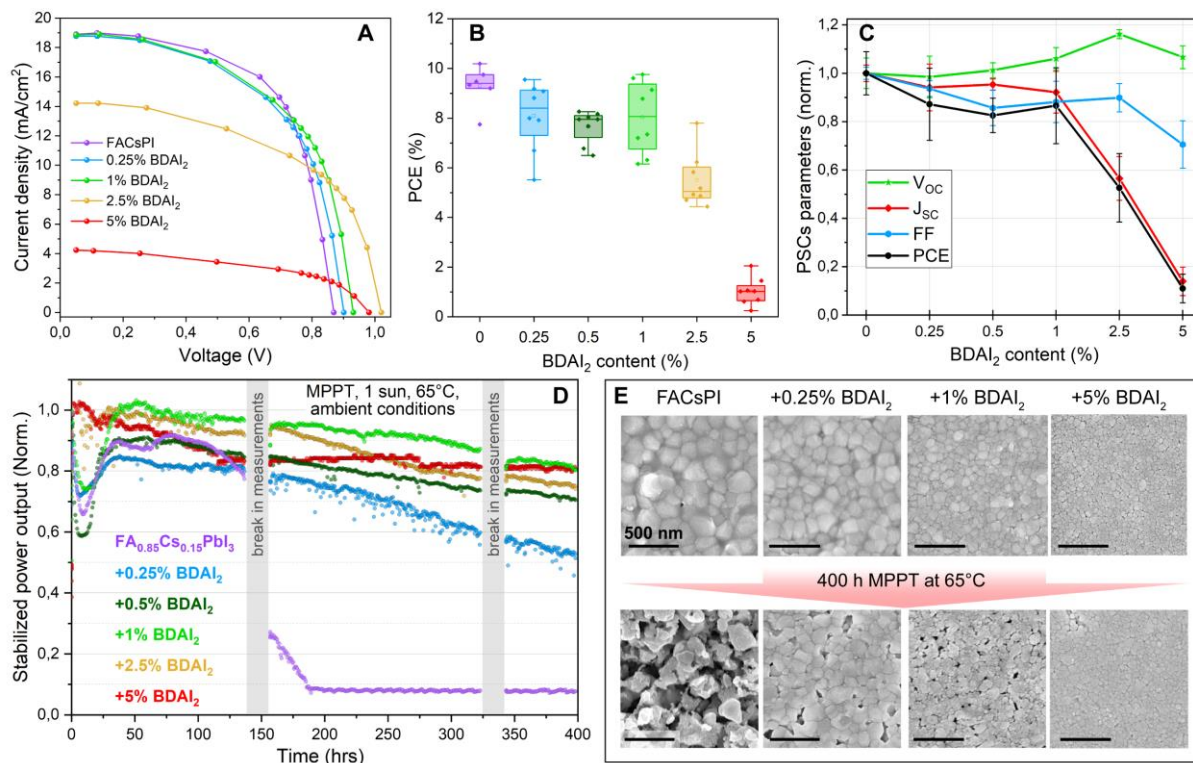


Figure 5. (A) Quasi-steady-state J–V curves of record FA_{0.85}Cs_{0.15}PbI₃-based devices with 0.25, 1, 2.5, and 5% BDAI₂ additive. (B) Distribution of absolute PCE values of FA_{0.85}Cs_{0.15}PbI₃-based PSCs with a different BDAI₂ content. (C) The dependence of FF, V_{OC}, J_{SC}, and PCE parameters as a function of BDAI₂ content. Each parameter is normalized by the corresponding average value of the reference devices. (D) Normalized values of stabilized power output (SPO) of encapsulated devices with a different BDAI₂ amount. Vertical grey regions illustrate the technical interruptions in signal registration. During this time, light soaking and heating did not stop; the devices were loaded at a voltage near the MPP conditions. (E) SEM images of FACsPI + x% BDAI₂ perovskite surface in PSCs before (top row) and after 400 h of MPPT at 65 °C (bottom row). All scale bars correspond to 500 nm.

We suppose that the mechanism of PSC stability increase with BDAI₂ passivation could originate from the intergrain “encapsulation” by either (BDA)PbI₄ phases or BDA²⁺ monolayers and the additional improvement of the interconnection between perovskite grains, owing to bidentate diammonium cations. This hypothesis is primarily supported by the electron microscopy data (Figure 5E), as well as by the increasing values of shunt resistance in the passivated devices (Figure S7). The presence of diammonium passivation at the GBs, which are known to be the main channels of ion migration [52], could also decrease the extent of extrinsic and intrinsic ionic migration—the main factor of potential-induced degradation in various types of solar cells, including PSCs [53].

4. Conclusions

In conclusion, we experimentally demonstrated that (BDA)PbI₄ is the only stable 2D perovskite phase based on 1,4-butanediammonium cations, which means that (BDA)(MA)_{n-1}Pb_nI_{3n+1} compositional row is not suitable for the use as phase-pure light-harvesting materials in PSCs. The bulk passivation of 3D ABX₃ hybrid perovskites with

BDAI₂ leads to the modulation of the perovskites' microstructure and optoelectronic properties depending on the amount of diammonium additive. BDA²⁺ cations seem to accumulate mostly on the perovskite grain boundaries in the form of either (BDA)PbI₄ phases or BDA²⁺-containing layers, leading to the gradual decrease in the average grain size with an increased BDAI₂ content. No phase impurities were detected in the passivated samples. The influence of BDAI₂ passivation on perovskite optoelectronic properties and device performance demonstrates a threshold behavior with a positive effect on perovskite materials below the threshold (increase in PL intensity, charge carrier lifetimes, V_{OC}; shunt resistance) and a strongly negative effect above the threshold (decrease in PL intensity and charge carrier lifetimes, J_{SC} decrease; series resistance increase). In the case of BDAI₂, the threshold value was found to be ~ 1 mol.% for FACsPI and ~ 0.5 mol.% for MAFAPI compositions, with respect to Pb content. On the other hand, the presence of any amount of diammonium salt leads to the sufficient enhancement of the photothermal stability of perovskite materials and devices, compared to the reference samples. The performance of the passivated devices remained within the 50 to 80% range of the initial PCE after 400 h of continuous 1 sun irradiation with a stabilized temperature of 65 °C, while the performance of the control devices deteriorated after 170 h of the experiment. The most possible stabilization mechanism of BDAI₂-passivated PSCs is assumed to originate from the intergrain encapsulation by either (BDA)PbI₄ phases or BDA²⁺ monolayers and the additional improvement of interconnection between perovskite grains, owing to bidentate diammonium cations. Therefore, 1,4-butanediammonium iodide could be considered as a promising additive for the improvement of PSC stability, but the amount of this salt should be carefully controlled to improve the performance of the final devices.

Supplementary Materials: The following supporting information can be downloaded at <https://www.mdpi.com/article/10.3390/nano12244357/s1>: Figure S1: XRD patterns of 2D perovskites, prepared from (BDA)(MA)Pb₂I₇ solutions with different concentrations; Figure S2: XRD patterns of 2D perovskite crystals, prepared from (BDA)(MA)Pb₂I₇ solutions with different excess amounts of MAI; Figure S3: XRD patterns of FA_{0.85}Cs_{0.15}PbI₃ perovskite films with different BDAI₂ contents; Figure S4: SEM images of FACsPI perovskite films with different BDAI₂ contents; Figure S5: Tauc plots of FA_{0.85}Cs_{0.15}PbI₃ perovskite films with different BDAI₂ contents; Figure S6: Distributions of operando parameters of PSCs based on FACsPI + x% BDAI₂ light-harvesting materials; Figure S7: The dependence of R_{series} and R_{shunt} of PSCs on BDAI₂ content; Figure S8: Absolute SPO values of encapsulated perovskite solar cells with different BDAI₂ amounts under continuous 1 sun illumination, stabilized temperature of 65 °C, and ambient environment; Figure S9: SEM images of FACsPI perovskite films with different BDAI₂ contents before and after 400 h of PSC photothermal aging.

Author Contributions: Conceptualization, N.N.U., A.K.M., E.A.G. and A.B.T.; methodology, N.N.U., A.K.M., N.A.B., A.S.T. and P.A.I.; writing—original draft preparation, N.N.U. and A.K.M.; writing—review and editing, N.N.U., A.B.T. and E.A.G.; visualization, N.N.U. and A.K.M.; supervision, A.B.T. and E.A.G. All authors have read and agreed to the published version of the manuscript.

Funding: This research was funded by the Russian Science Foundation, project number 19-73-30022.

Data Availability Statement: Not applicable.

Acknowledgments: XRD and SEM studies were performed using the equipment provided by the Joint Research Centre for Physical Methods of Research of the Kurnakov Institute of General and Inorganic Chemistry of the Russian Academy of Sciences (JRC PMR IGIC RAS).

Conflicts of Interest: The authors declare no conflict of interest.

References

1. NREL Best Research-Cell Efficiencies. NREL. Available online: <https://www.nrel.gov/pv/cell-efficiency.html> (accessed on 12 November 2022).
2. Khenkin, M.V.; Katz, E.A.; Abate, A.; Bardizza, G.; Berry, J.J.; Brabec, C.; Brunetti, F.; Bulović, V.; Burlingame, Q.; Di Carlo, A.; et al. Consensus Statement for Stability Assessment and Reporting for Perovskite Photovoltaics Based on ISOS Procedures. *Nat. Energy* **2020**, *5*, 35–49. [CrossRef]

3. Poorkazem, K.; Kelly, T.L. Compositional Engineering To Improve the Stability of Lead Halide Perovskites: A Comparative Study of Cationic and Anionic Dopants. *ACS Appl. Energy Mater.* **2018**, *1*, 181–190. [[CrossRef](#)]
4. Rakstys, K.; Igci, C.; Nazeeruddin, M.K. Efficiency vs. Stability: Dopant-Free Hole Transporting Materials towards Stabilized Perovskite Solar Cells. *Chem. Sci.* **2019**, *10*, 6748–6769. [[CrossRef](#)]
5. Zhang, S.; Liu, Z.; Zhang, W.; Jiang, Z.; Chen, W.; Chen, R.; Huang, Y.; Yang, Z.; Zhang, Y.; Han, L.; et al. Barrier Designs in Perovskite Solar Cells for Long-Term Stability. *Adv. Energy Mater.* **2020**, *10*, 1–49. [[CrossRef](#)]
6. Ahmad, S.; Fu, P.; Yu, S.; Yang, Q.; Liu, X.; Wang, X.; Wang, X.; Guo, X.; Li, C. Dion-Jacobson Phase 2D Layered Perovskites for Solar Cells with Ultrahigh Stability. *Joule* **2019**, *3*, 794–806. [[CrossRef](#)]
7. Grancini, G.; Roldán-Carmona, C.; Zimmermann, I.; Mosconi, E.; Lee, X.; Martineau, D.; Narbey, S.; Oswald, F.; De Angelis, F.; Graetzel, M.; et al. One-Year Stable Perovskite Solar Cells by 2D/3D Interface Engineering. *Nat. Commun.* **2017**, *8*, 15684. [[CrossRef](#)]
8. Li, Y.; Wu, H.; Qi, W.; Zhou, X.; Li, J.; Cheng, J.; Zhao, Y.; Li, Y.; Zhang, X. Passivation of Defects in Perovskite Solar Cell: From a Chemistry Point of View. *Nano Energy* **2020**, *77*, 105237. [[CrossRef](#)]
9. Zhang, Z.; Wu, J.; Li, S.; Liu, S.; Wang, Q.; Mei, A.; Rong, Y.; Han, H.; Hu, Y. Progress in Multifunctional Molecules for Perovskite Solar Cells. *Sol. RRL* **2020**, *4*, 1–17. [[CrossRef](#)]
10. Alharbi, E.A.; Alyamani, A.Y.; Kubicki, D.J.; Uhl, A.R.; Walder, B.J.; Alanazi, A.Q.; Luo, J.; Burgos-Caminal, A.; Albadri, A.; Albrithen, H.; et al. Atomic-Level Passivation Mechanism of Ammonium Salts Enabling Highly Efficient Perovskite Solar Cells. *Nat. Commun.* **2019**, *10*, 1–9. [[CrossRef](#)]
11. Wu, S.; Zhang, J.; Li, Z.; Liu, D.; Qin, M.; Cheung, S.H.; Lu, X.; Lei, D.; So, S.K.; Zhu, Z.; et al. Modulation of Defects and Interfaces through Alkylammonium Interlayer for Efficient Inverted Perovskite Solar Cells. *Joule* **2020**, *4*, 1248–1262. [[CrossRef](#)]
12. Stoumpos, C.C.; Cao, D.H.; Clark, D.J.; Young, J.; Rondinelli, J.M.; Jang, J.I.; Hupp, J.T.; Kanatzidis, M.G. Ruddlesden–Popper Hybrid Lead Iodide Perovskite 2D Homologous Semiconductors. *Chem. Mater.* **2016**, *28*, 2852–2867. [[CrossRef](#)]
13. Gharibzadeh, S.; Abdollahi Nejad, B.; Jakoby, M.; Abzieher, T.; Hauschild, D.; Moghadamzadeh, S.; Schwenzer, J.A.; Brenner, P.; Schmager, R.; Haghighirad, A.A.; et al. Record Open-Circuit Voltage Wide-Bandgap Perovskite Solar Cells Utilizing 2D/3D Perovskite Heterostructure. *Adv. Energy Mater.* **2019**, *9*, 1–10. [[CrossRef](#)]
14. Sidhik, S.; Wang, Y.; de Siena, M.; Asadpour, R.; Torma, A.; Terlier, T.; Ho, K.; Li, W.; Puthirath, A.B.; Shuai, X.; et al. Deterministic Fabrication of 3D/2D Perovskite Bilayer Stacks for Durable and Efficient Solar Cells. *Science* **2022**, *1430*, 1425–1430. [[CrossRef](#)] [[PubMed](#)]
15. Fiorentino, F.; Albaqami, M.D.; Poli, I.; Petrozza, A. Thermal- and Light-Induced Evolution of the 2D/3D Interface in Lead-Halide Perovskite Films. *ACS Appl. Mater. Interfaces* **2022**, *14*, 34180–34188. [[CrossRef](#)] [[PubMed](#)]
16. Sutanto, A.A.; Szostak, R.; Drigo, N.; Quelo, V.I.E.; Marchezi, P.E.; Germino, J.C.; Tolentino, H.C.N.; Nazeeruddin, M.K.; Nogueira, A.F.; Grancini, G. In Situ Analysis Reveals the Role of 2D Perovskite in Preventing Thermal-Induced Degradation in 2D/3D Perovskite Interfaces. *Nano Lett.* **2020**, *20*, 3992–3998. [[CrossRef](#)] [[PubMed](#)]
17. Wu, W.Q.; Yang, Z.; Rudd, P.N.; Shao, Y.; Dai, X.; Wei, H.; Zhao, J.; Fang, Y.; Wang, Q.; Liu, Y.; et al. Bilateral Alkylamine for Suppressing Charge Recombination and Improving Stability in Blade-Coated Perovskite Solar Cells. *Sci. Adv.* **2019**, *5*, eaav8925. [[CrossRef](#)]
18. Ma, C.; Shen, D.; Ng, T.-W.; Lo, M.-F.; Lee, C.-S. 2D Perovskites with Short Interlayer Distance for High-Performance Solar Cell Application. *Adv. Mater.* **2018**, *30*, 1800710. [[CrossRef](#)]
19. Jiang, X.; Zhang, J.; Ahmad, S.; Tu, D.; Liu, X.; Jia, G.; Guo, X.; Li, C. Dion-Jacobson 2D-3D Perovskite Solar Cells with Improved Efficiency and Stability. *Nano Energy* **2020**, *75*, 104892. [[CrossRef](#)]
20. Zhong, Y.; Liu, G.; Su, Y.; Sheng, W.; Gong, L.; Zhang, J.; Tan, L.; Chen, Y. Diammonium Molecular Configuration-Induced Regulation of Crystal Orientation and Carrier Dynamics for Highly Efficient and Stable 2D/3D Perovskite Solar Cells. *Angew. Chemie-Int. Ed.* **2022**, *61*. [[CrossRef](#)]
21. Zheng, Y.; Niu, T.; Qiu, J.; Chao, L.; Li, B.; Yang, Y.; Li, Q.; Lin, C.; Gao, X.; Zhang, C.; et al. Oriented and Uniform Distribution of Dion–Jacobson Phase Perovskites Controlled by Quantum Well Barrier Thickness. *Sol. RRL* **2019**, *3*, 1–9. [[CrossRef](#)]
22. Liu, S.; Guan, X.; Xiao, W.; Chen, R.; Zhou, J.; Ren, F.; Wang, J.; Chen, W.; Li, S.; Qiu, L.; et al. Effective Passivation with Size-Matched Alkyldiammonium Iodide for High-Performance Inverted Perovskite Solar Cells. *Adv. Funct. Mater.* **2022**, *32*, 1–12. [[CrossRef](#)]
23. Ahmad, S.; Lu, R.; Liu, Y.; Liu, X.; Yang, Q.; Guo, X.; Li, C. Cesium-Doped Dion-Jacobson 2D Perovskites for Highly Stable Photovoltaics with an 18.3% Efficiency. *Nano Energy* **2022**, *103*, 107822. [[CrossRef](#)]
24. Zhang, F.; Park, S.Y.; Yao, C.; Lu, H.; Dunfield, S.P.; Xiao, C.; Uličná, S.; Zhao, X.; Hill, L.D.; Chen, X.; et al. Metastable Dion–Jacobson 2D Structure Enables Efficient and Stable Perovskite Solar Cells. *Science* **2022**, *375*, 71–76. [[CrossRef](#)] [[PubMed](#)]
25. Fateev, S.A.; Petrov, A.A.; Ordinartsev, A.A.; Grishko, A.Y.; Goodilin, E.A.; Tarasov, A.B. Universal Strategy of 3D and 2D Hybrid Perovskites Single Crystal Growth via In Situ Solvent Conversion. *Chem. Mater.* **2020**, *32*, 9805–9812. [[CrossRef](#)]
26. Saliba, M.; Correa-Baena, J.P.; Wolff, C.M.; Stolterfoht, M.; Phung, N.; Albrecht, S.; Neher, D.; Abate, A. How to Make over 20% Efficient Perovskite Solar Cells in Regular (n-i-p) and Inverted (p-i-n) Architectures. *Chem. Mater.* **2018**, *30*, 4193–4201. [[CrossRef](#)]
27. Belich, N.A.; Petrov, A.A.; Ivlev, P.A.; Udalova, N.N.; Pustovalova, A.A.; Goodilin, E.A.; Tarasov, A.B. How to Stabilize Standard Perovskite Solar Cells to Withstand Operating Conditions under an Ambient Environment for More than 1000 Hours Using Simple and Universal Encapsulation. *J. Energy Chem.* **2022**. *Just accepted*.

28. Udalova, N.N.; Fateev, S.A.; Nemygina, E.M.; Zanetta, A.; Grancini, G.; Goodilin, E.A.; Tarasov, A.B. Nonmonotonic Photostability of BA2MAn-1PbnI3 N+1 Homologous Layered Perovskites. *ACS Appl. Mater. Interfaces* **2022**, *14*, 961–970. [[CrossRef](#)]
29. Motti, S.G.; Meggiolaro, D.; Barker, A.J.; Mosconi, E.; Perini, C.A.R.; Ball, J.M.; Gandini, M.; Kim, M.; De Angelis, F.; Petrozza, A. Controlling Competing Photochemical Reactions Stabilizes Perovskite Solar Cells. *Nat. Photonics* **2019**, *13*, 532–539. [[CrossRef](#)]
30. Wang, H.; Chan, C.C.S.; Chu, M.; Xie, J.; Zhao, S.; Guo, X.; Miao, Q.; Wong, K.S.; Yan, K.; Xu, J. Interlayer Cross-Linked 2D Perovskite Solar Cell with Uniform Phase Distribution and Increased Exciton Coupling. *Sol. RRL* **2020**, *4*, 1–9. [[CrossRef](#)]
31. Li, X.; Hoffman, J.; Ke, W.; Chen, M.; Tsai, H.; Nie, W.; Mohite, A.D.; Kepenekian, M.; Katan, C.; Even, J.; et al. Two-Dimensional Halide Perovskites Incorporating Straight Chain Symmetric Diammonium Ions, (NH₃CmH₂mNH₃)(CH₃NH₃)N–1PbnI_{3n+1} (m = 4–9; n = 1–4). *J. Am. Chem. Soc.* **2018**, *140*, 12226–12238. [[CrossRef](#)]
32. Zhou, Z.; Yang, S.; Xu, K.; Qiao, H.W.; Xie, J.; Lin, Z.; Ge, B.; He, J.; Chen, M.; Zhang, J.; et al. Diammonium-Cesium Lead Halide Perovskite with Phase-Segregated Interpenetrating Morphology for Photovoltaics. *J. Phys. Chem. Lett.* **2020**, *11*, 747–754. [[CrossRef](#)] [[PubMed](#)]
33. Yao, Z.; Zhou, Y.; Yin, X.; Li, X.; Han, J.; Tai, M.; Zhou, Y.; Li, J.; Hao, F.; Lin, H. Role of Alkyl Chain Length in Diaminoalkane Linked 2D Ruddlesden-Popper Halide Perovskites. *CrystEngComm* **2018**, *20*, 6704–6712. [[CrossRef](#)]
34. Marchenko, E.I.; Fateev, S.A.; Petrov, A.A.; Korolev, V.V.; Mitrofanov, A.; Petrov, A.V.; Goodilin, E.A.; Tarasov, A.B. Database of Two-Dimensional Hybrid Perovskite Materials: Open-Access Collection of Crystal Structures, Band Gaps, and Atomic Partial Charges Predicted by Machine Learning. *Chem. Mater.* **2020**, *32*, 7383–7388. [[CrossRef](#)]
35. Lemmerer, A.; Billing, D.G. Lead Halide Inorganic-Organic Hybrids Incorporating Diammonium Cations. *CrystEngComm* **2012**, *14*, 1954–1966. [[CrossRef](#)]
36. Belich, N.A.; Petrov, A.A.; Rudnev, P.O.; Stepanov, N.M.; Turkevych, I.; Goodilin, E.A.; Tarasov, A.B. From Metallic Lead Films to Perovskite Solar Cells through Lead Conversion with Polyhalide Solutions. *ACS Appl. Mater. Interfaces* **2020**, *12*, 20456–20461. [[CrossRef](#)]
37. Petrov, A.A.; Belich, N.A.; Grishko, A.Y.; Stepanov, N.M.; Dorofeev, S.G.; Maksimov, E.G.; Shevelkov, A.V.; Zakeeruddin, S.M.; Graetzel, M.; Tarasov, A.B.; et al. A New Formation Strategy of Hybrid Perovskites via Room Temperature Reactive Polyiodide Melts. *Mater. Horiz.* **2017**, *4*, 625–632. [[CrossRef](#)]
38. Zhao, T.; Chueh, C.C.; Chen, Q.; Rajagopal, A.; Jen, A.K.Y. Defect Passivation of Organic-Inorganic Hybrid Perovskites by Diammonium Iodide toward High-Performance Photovoltaic Devices. *ACS Energy Lett.* **2016**, *1*, 757–763. [[CrossRef](#)]
39. Wang, X.; Zhao, Y.; Li, B.; Han, X.; Jin, Z.; Wang, Y.; Zhang, Q.; Rui, Y. Interfacial Modification via a 1,4-Butanediamine-Based 2D Capping Layer for Perovskite Solar Cells with Enhanced Stability and Efficiency. *ACS Appl. Mater. Interfaces* **2022**, *14*, 22879–22888. [[CrossRef](#)]
40. Li, W.; Gu, X.; Shan, C.; Lai, X.; Sun, X.W.; Kyaw, A.K.K. Efficient and Stable Mesoscopic Perovskite Solar Cell in High Humidity by Localized Dion-Jacobson 2D-3D Heterostructures. *Nano Energy* **2022**, *91*, 106666. [[CrossRef](#)]
41. Leijtens, T.; Bush, K.; Cheacharoen, R.; Beal, R.; Bowering, A.; McGehee, M.D. Towards Enabling Stable Lead Halide Perovskite Solar Cells; Interplay between Structural, Environmental, and Thermal Stability. *J. Mater. Chem. A* **2017**, *5*, 11483–11500. [[CrossRef](#)]
42. Correa-Baena, J.-P.; Saliba, M.; Buonassisi, T.; Grätzel, M.; Abate, A.; Tress, W.; Hagfeldt, A. Promises and Challenges of Perovskite Solar Cells. *Science* **2017**, *358*, 739–744. [[CrossRef](#)] [[PubMed](#)]
43. Xiao, J.W.; Liu, L.; Zhang, D.; De Marco, N.; Lee, J.W.; Lin, O.; Chen, Q.; Yang, Y. The Emergence of the Mixed Perovskites and Their Applications as Solar Cells. *Adv. Energy Mater.* **2017**, *7*, 1–24. [[CrossRef](#)]
44. Ono, L.K.; Juarez-Perez, E.J.; Qi, Y. Progress on Perovskite Materials and Solar Cells with Mixed Cations and Halide Anions. *ACS Appl. Mater. Interfaces* **2017**, *9*, 30197–30246. [[CrossRef](#)] [[PubMed](#)]
45. Chen, Z.; Zheng, X.; Yao, F.; Ma, J.; Tao, C.; Fang, G. Methylammonium, Formamidinium and Ethylenediamine Mixed Triple-Cation Perovskite Solar Cells with High Efficiency and Remarkable Stability. *J. Mater. Chem. A* **2018**, *6*, 17625–17632. [[CrossRef](#)]
46. Lu, J.; Jiang, L.; Li, W.; Li, F.; Pai, N.K.; Scully, A.D.; Tsai, C.M.; Bach, U.; Simonov, A.N.; Cheng, Y.B.; et al. Diammonium and Monoammonium Mixed-Organic-Cation Perovskites for High Performance Solar Cells with Improved Stability. *Adv. Energy Mater.* **2017**, *7*, 1–10. [[CrossRef](#)]
47. Stolterfoht, M.; Wolff, C.M.; Márquez, J.A.; Zhang, S.; Hages, C.J.; Rothhardt, D.; Albrecht, S.; Burn, P.L.; Meredith, P.; Unold, T.; et al. Visualization and Suppression of Interfacial Recombination for High-Efficiency Large-Area Pin Perovskite Solar Cells. *Nat. Energy* **2018**, *3*, 847–854. [[CrossRef](#)]
48. Uller Rothmann, M.; Kim, J.S.; Borchert, J.; Lohmann, K.B.; O’Leary, C.M.; Sheader, A.A.; Clark, L.; Snaith, H.J.; Johnston, M.B.; Nellist, P.D.; et al. Atomic-Scale Microstructure of Metal Halide Perovskite. *Science* **2020**, *370*, eabb5940. [[CrossRef](#)]
49. Chen, J.; Seo, J.Y.; Park, N.G. Simultaneous Improvement of Photovoltaic Performance and Stability by In Situ Formation of 2D Perovskite at (FAPbI₃)_{0.88}(CsPbBr₃)_{0.12}/CuSCN Interface. *Adv. Energy Mater.* **2018**, *8*, 1–15. [[CrossRef](#)]
50. Jung, E.H.; Jeon, N.J.; Park, E.Y.; Moon, C.S.; Shin, T.J.; Yang, T.-Y.Y.; Noh, J.H.; Seo, J. Efficient, Stable and Scalable Perovskite Solar Cells Using Poly(3-Hexylthiophene). *Nature* **2019**, *567*, 511–515. [[CrossRef](#)]
51. Bai, Y.; Huang, Z.; Zhang, X.; Lu, J.; Niu, X.; He, Z.; Zhu, C.; Xiao, M.; Song, Q.; Wei, X.; et al. Initializing Film Homogeneity to Retard Phase Segregation for Stable Perovskite Solar Cells. *Science* **2022**, *754*, 747–754. [[CrossRef](#)]

-
52. Yuan, Y.; Huang, J. Ion Migration in Organometal Trihalide Perovskite and Its Impact on Photovoltaic Efficiency and Stability. *Acc. Chem. Res.* **2016**, *49*, 286–293. [[CrossRef](#)] [[PubMed](#)]
 53. Xu, L.; Liu, J.; Luo, W.; Wehbe, N.; Seikhan, A.; Babics, M.; Kang, J.; De Bastiani, M.; Aydin, E.; Allen, T.G.; et al. Potential-Induced Degradation in Perovskite/Silicon Tandem Photovoltaic Modules. *Cell Reports Phys. Sci.* **2022**, *3*, 101026. [[CrossRef](#)]